SCIENTIFIC NOTEBOOK 618E
VOLUME 1
VOLUME 2

DANI OR

Volume 1:
Seepage Threshold into Subterranean Openings in Fractured Rock (Continuation for Scientific Notebook #354)

Account Number: 20.06002.01.131 (USFIC KTI)
Collaborators: Markus Tuller (USU), Randall Fedors (CNWRA)
Directories: C:\SCI_NOTE_SEEPAGE\

Objectives: Documentation of development and evaluation of a theoretical model for prediction of seepage rates into YM drift for a range of background percolation rates (fluxes). The documentation includes: (1) a brief review of the Or and Tuller [2003] unsaturated hydraulic conductivity relationships for fractured porous media; (2) theoretical considerations and derivations to estimate the seepage fraction as a function of percolation flux; (3) a comparison with the Finsterle [2000] model calculations; and (4) a sensitivity analysis to establish potential bounds for seepage rates.

Dani Or

07/05/04 – Initial entry (notebook continuation)

- The basic idea is to develop a physically-based alternative to the numerically-based predictions of seepage exclusions proposed by Finsterle and coworkers. We perceive the lack of a strong connection to the physics of seepage by these models, and the disconnect of injection tests performed at percolation rates and conditions not entirely consistent with the expected ambient environment, the predicative capability of the FCM for locations across the potential repository may be highly uncertain.
- We plan to separate the contributions of matrix and fracture to seepage based on theoretical and practical arguments.
- Estimation of seepage into cavities intersected by vertical fractures will be based on the following key steps - first, we establish that for rock properties prevailing at Yucca Mountain (and probably other fractured rock), seepage is more likely to originate from fractures intersecting the cavities than from rock matrix itself. Next, we consider flow in the matrix and on fracture surfaces to derive estimates of the effective permeability of the fractured rock mass as a function of background flux (and matric potential). Finally, considering negligible matrix component of seepage (due to restraining capillary forces), we focus on flow through fractures intersecting the opening. We plot the unsaturated hydraulic conductivity of the fracture domain weighted by fracture porosity as a function of background flux to obtain estimates of seepage for a range of percolation fluxes.
- The proposed approach views the fractured rock as discrete fractures overprinted on a classical porous matrix (Fig. 1). The capillary barrier presented by the cavity walls reduces seepage, hence incoming water flux in the matrix is diverted around the cavity. In contrast, water in large aperture fractures would seep through gravity assisted film flow, possibly leading to drop formation and dripping [Or and Ghezzehei, 2000]. Thus, the approach is not sensitive to cavity geometry. Effect of fracture orientation on potential interception of laterally diverted water flux is neglected.

Large subterranean cavities and drifts excavated in porous media may interrupt and potentially divert the steady downward water flux found at large depths. The presence of a cavity wall introduces a large capillary discontinuity that could prevent water from seeping into the cavity depending on the magnitude of the water flux, porous media properties, and the shape of the cavity surface [Ross, 1990; Selker, 1997]. To minimize unwanted seepage, these dependencies may be gainfully exploited for the design of subsurface waste repositories such as for the potential repository for high-level nuclear waste at Yucca Mountain, Nevada. Analytical solutions for seepage diversion around cavities in homogeneous porous

media under steady state conditions have been developed by Knight et al. [1989] Philip et al. [1989], and Philip [1990]. A key assumption in these analyses is that of a homogeneous porous medium, as stated in Philip et al. [1989]: "Our analyses are developed for homogeneous media…They do not, of course, accommodate small-scale heterogeneity in the immediate neighborhood of the hole(s)". The role of small scale irregularities in cavity surfaces was subsequently investigated by Hughson and Dodge [2000] showing they may significantly reduce seepage threshold into the cavity.

In some cases, the prediction of seepage behavior into cavities formed in fractured porous media presents additional challenges. Finsterle [2000] and Finsterle et al. [2003] conducted a series of numerical studies to help quantify seepage into underground openings excavated in fractured rock. The numerical studies intended to support the calibration of their numerical model using data collected at a number of water injection experiments at Yucca Mountain [BSC, 2003a]. They compared prediction of seepage behavior using fracture continuum representation (FCM) of the heterogeneous medium with results from a detailed discrete fracture (feature) model (DFM) that preserves the main features of a hypothetical fracture network by approximating fractures as wide bands using lines of grid cells in a single continuum, equivalent porous media model. Finsterle et al. [2003] endorsed the use of a simplified FCM based on the practical need of providing estimates of average seepage over a range of background percolation fluxes to support performance assessment, design, and engineering evaluations associated with waste emplacement drifts in unsaturated fractured rock. Although the argument for simplicity by homogenization of porous media properties is appealing, and the proposition for developing "a physically-based process model using effective parameters that are directly determined from seepage experiments" [Finsterle et al., 2003] appears reasonable, the implementation is hampered by unnecessary oversimplified depiction of key physical processes governing seepage in fractured rock. With the lack of a strong connection to the physics of seepage, and the disconnect with injection tests performed at percolation rates and conditions not consistent with ambient environment, the predicative capability of the FCM for locations across the potential repository may be highly uncertain.

The objective of this study was to present a simple and physically-based modeling alternative for establishing estimates of seepage rates into large cavities in fractured rock considering a wide range of background fluxes. We attempt to preserve the physics of flow in unsaturated fractures by considering the role of film flow along fracture surfaces, and capitalizing on demonstrably large disparity between matrix and fracture pore spaces (Fig.1). In contrast with numerical DFM analyses examined by Finsterle et al. [2003] and others, the proposed approach requires limited information on fractures (aperture distribution and porosity for fractures intersecting the cavity) and does not rely on fracture network topology that is often cited as the most significant impediment to detailed DFM modeling [Finsterle, 2000]. The fractured rock is represented as a dual-continuum reflecting the two disparate populations of matrix pores and fracture apertures and a few aspects of fracture surface roughness as described in Or and Tuller [2000 and 2003].

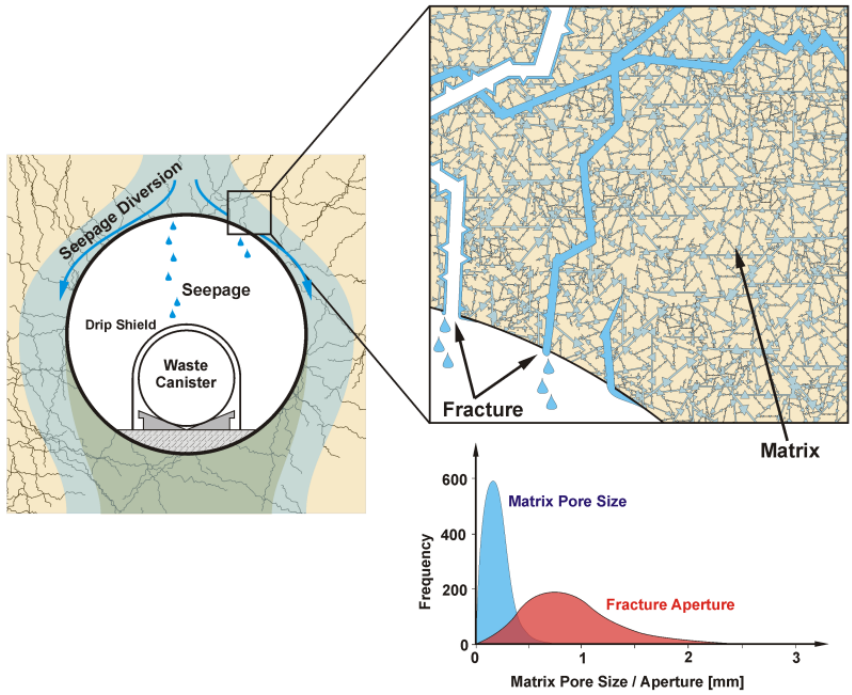

Fig.1: Definition sketch for seepage exclusion around a cylindrical cavity and depiction of fractured porous medium pore space and size distributions.

07/12/04 - Modeling flow in unsaturated fractured porous media (FPM)

In the following we review key aspects related to modeling flow in unsaturated FPM [Or and Tuller, 2003]. Details are presented in the previous notebook.

Models for equilibrium liquid-vapor interfacial configurations in fractured porous media enable detailed liquid retention modeling and provide boundary conditions for hydrodynamic considerations. The fractured rock pore space is represented by a bimodal distribution of pores reflecting the two disparate populations of matrix pores and fracture apertures (Fig.1). Additionally, fracture surface roughness is included and represented by a distribution of angular pits and grooves [Or and Tuller, 2000]. Following the derivations in Or and Tuller [2003] and justification therein, flow pathways are calculated for 2-D cross section perpendicular to downward flow neglecting 3-D network effects. This representation emphasizes the flow behavior and capacity of fracture traces intersecting cavity surfaces (as two dimensional projections), and neglects both seepage enhancement due to axially-oriented fractures or lateral diversion of fracture in the transverse direction.

For flow processes within a partially saturated FPM cross-section (Fig.2a) we assume that equilibrium liquid-vapor interfaces remain stable under relatively slow and laminar flow conditions. In accordance with different potential liquid filling stages of a unit fracture element discussed in Or and Tuller [2003] we consider four laminar flow regimes (Fig.2b). When the fracture element is completely liquid-filled (or saturated), we consider flow between parallel plates (defined by nominal aperture width, B) supplemented by flow in isosceles triangular ducts (surface grooves). For partially filled fracture elements, we invoke the interfacial stability assumption and consider laminar flow in corners (surface grooves) bounded by a liquid-vapor interface, and flow in adsorbed films lining all other fracture surfaces [Tokunaga and Wan, 1997]. For the derivation of macroscopic hydraulic conductivity it is not necessary to describe details of the velocity fields; instead, the average flow velocities associated with these flow regimes are sufficient. Solutions of the Navier-Stokes equation for each flow regime and geometry are given in Or and Tuller [2003]. Hydraulic conductivities for each flow regime in a unit fracture element are derived by substituting

average fluid velocity from the Navier-Stokes equation into Darcy's law and considering a unit pressure gradient along the flow path [Tuller and Or, 2001].

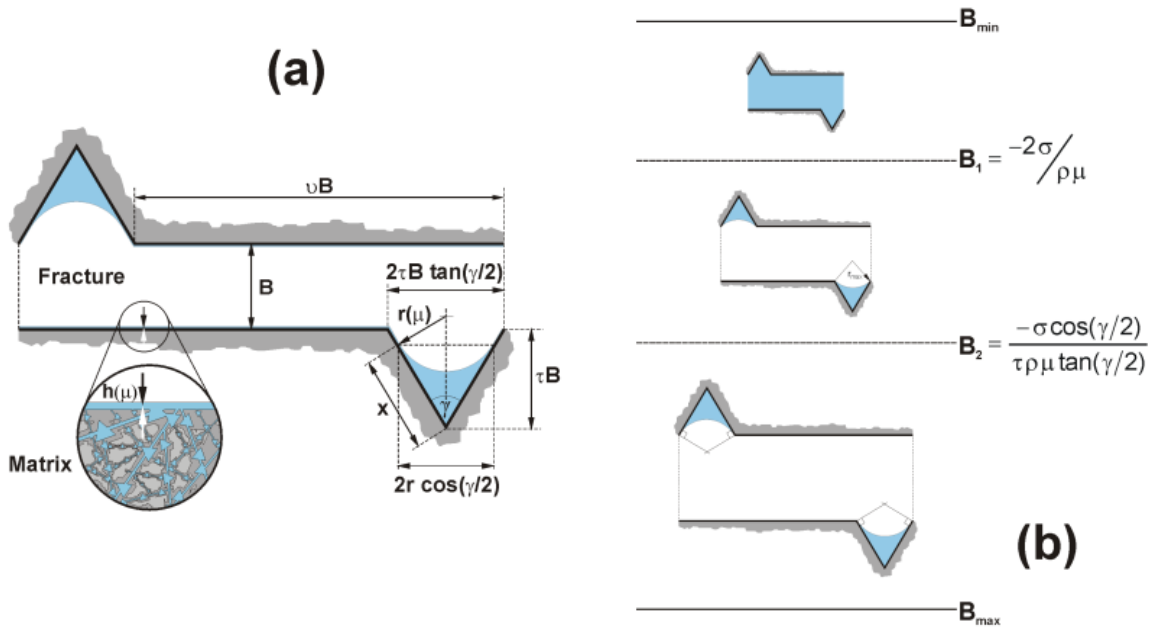

Fig.2: (a) Definition sketch for a unit fracture element representing a partially saturated fracture with liquid retained in crevices and adsorbed liquid films; (b) Critical aperture sizes determining expected fracture-filling stages at different matric potentials.

The hydraulic conductivity of a unit fracture element is then assembled by weighting the hydraulic conductivities of each flow regime by their associated liquid occupied cross-sectional areas and dividing the resulting expressions by the total cross-sectional area AT of the unit fracture element (including the matrix shell). This analysis yields three expressions for the hydraulic conductivity of a single unit fracture element at various filling stages given as:

Saturated hydraulic conductivity: $\mu > \mu_1$

$$K_1 = K_{SAT} = \frac{B^4\left(K_s\left(\nu + 2\tau\tan\left(\frac{\gamma}{2}\right)\right) + K_d\, 2\tau^2\,\delta\tan\left(\frac{\gamma}{2}\right)\right)}{A_T} \tag{1}$$

Separated interfaces – capillary menisci anchored at pit edges: $\mu_1 \geq \mu > \mu_2$

$$K_2(\mu) = \frac{KF(\mu)2\nu B h(\mu) + KC(\mu)\,\delta\left(2\tau B\tan\left(\frac{\gamma}{2}\right)\left(\tau B + \sqrt{r(\mu)^2 - \tau^2 B^2 \tan\left(\frac{\gamma}{2}\right)^2}\right) - 2r(\mu)^2\,\mathrm{asin}\left(\frac{\tau B\tan\left(\frac{\gamma}{2}\right)}{r(\mu)}\right)\right)}{A_T} \tag{2}$$

Separated interfaces – capillary menisci tangent pit surfaces: $\mu \leq \mu_2$

$$K_3(\mu) = \frac{2KF(\mu)h(\mu)\left(B\nu + \frac{2B\tau}{\cos\left(\frac{\gamma}{2}\right)} - \frac{2r(\mu)}{\tan\left(\frac{\gamma}{2}\right)}\right) + 2KC(\mu)\delta r(\mu)^2 F_\gamma}{A_T} \tag{3}$$

where Ks, Kd, KF(μ), and KC(m) are the basic hydraulic conductivities for parallel plates, isosceles triangular ducts, surface films, and corners bounded by curved liquid-vapor interfaces respectively, h(μ) and r(μ) are the film thickness and radius of interface curvature as a function of the matric potential ($\tilde{\mu}$) The geometrical dimensions of the fracture element cross-section (Fig.2a) are defined by parameters γ, υ, and B, and $0<\delta<1$ is a groove connectivity factor to account for partial groove or pit connectivity in the direction of flow [Or and Tuller, 2000]. The parameter δ ensures that isolated pits do not contribute to the hydraulic conductivity functions in Eqs.1 to 3. Fracture filling stages are determined by spontaneous liquid displacement processes occurring at critical matric potentials μ_1 and μ_2.

A framework similar to the one described here was instrumental in deriving pore scale expressions for liquid retention and hydraulic conductivity for matrix pore space comprised of angular central pores connected to slit-shaped spaces [see Or and Tuller, 1999; and Tuller and Or, 2001].

For representation of FPM hydraulic properties at the sample scale, we employ a statistical upscaling scheme that assumes a bimodal distribution for matrix pore sizes and fracture apertures accounting for the two disparate pore populations and porosity as depicted in Fig.1.

The individual contributions of matrix pores and fractures to liquid saturation and unsaturated hydraulic conductivity are calculated separately, using the appropriate pore sizes and aperture distributions. The resultant saturation curves are weighted by the porosities of the respective domains and summed up to obtain the composite medium response. A similar approach was taken by Wang and Narasimhan [1993] in their Eqs.7.3.3 and 7.3.4 to represent the composite liquid retention and hydraulic conductivity functions for the fracture and matrix domains.

In the following we briefly explain the upscaling scheme for the fracture domain. We employ a statistical gamma distribution to represent the positive skewness often observed in fracture aperture size distributions [Chen and Kinzelbach, 2002; Bertels et al., 2001; Fischer et al., 1998; Pruess and Tsang, 1990; Wang and Narasimhan, 1993]. Sample-scale expressions for unsaturated hydraulic conductivity are obtained by taking expectations or integrating pore scale expressions (Eqs.1 to 3) with the gamma distribution over portions of the fracture population associated with a particular filling stage. The integration limits separating the fracture population are depicted in Fig.2b. Individual contributions of each fracture group in the population at a given potential are summed. The process is repeated for the entire matric potential range under consideration to yield the sample-scale saturation and hydraulic conductivity curves.

In the following example we illustrate the derivation of upscaled hydraulic conductivity (i.e., taking the expectation integral) for the fraction of the aperture population that is completely liquid-filled (in the size range from smallest aperture B_{min} to $B_1(\mu)$ in Fig.2b:

$$K_{1u-F}(\mu) = \int_{B_{min}}^{B_1(\mu)} \overbrace{\left[\frac{B^4\left(K_s\left(\nu + 2\tau\tan(\gamma/2)\right) + 2K_d\tau^2\tan(\gamma/2)\right)}{A_T}\right]}^{K_1 \text{ for a single fracture element (Eq.1)}} \overbrace{\left[\frac{B^2}{2\omega^3}\exp\left(-\frac{B}{\omega}\right)\right]}^{\text{Gamma distribution with } \xi=2} \quad dB \qquad (4)$$

with subscript u denoting “upscaled”, and F for “fracture”. Note that the saturated hydraulic conductivity for the entire fracture domain can be readily calculated using Eq.4 by simply changing the upper limit of integration to maximum aperture size B_{max}. The same procedure is applied to Eqs.2 and 3 with integration limits $B_1(\mu)$ to B_2, and B_2 to B_{max}, respectively. The upscaled expressions are then added to yield the composite response for the entire fracture population at a particular matric potential.

$$K_{u-F}(\mu) = \overbrace{K_{1u-F}(\mu)}^{\text{Eq.4}} + \overbrace{K_{2u-F}(\mu)}^{\text{upscaled Eq.2}} + \overbrace{K_{3u-F}(\mu)}^{\text{upscaled Eq.3}} \qquad (5)$$

For the matrix domain we employ a similar upscaling scheme yielding $K_{u-M}(\mu)$ [Tuller and Or, 2001]. The composite hydraulic conductivity curve is obtained by simple addition of the individual contributions of the matrix and fracture domains that are already normalized by their respective porosities (i.e., the individual expressions are already divided by total cross-sectional areas):

$$K_{FPM}(\mu) = K_{u-M}(\mu) + K_{u-F}(\mu) \tag{6}$$

Remark:

- The closed-form expressions for sample-scale hydraulic conductivity for the fracture and matrix domains were programmed in MS-Excel 2002. Sample work sheets (tsw35_fracture_master.xls and tsw35_matrix_master.xls) are archived under C:\SCI_NOTE_SEEPAGE\ . These files were also read by MS-Excel 97 SR-2, and no differences were found.

07/19/04 - Fracture Seepage and Rock Matrix Exclusion

In the following we present key steps for estimation of seepage into cylindrical cavities intersected by vertical fractures. First, we establish that for rock properties prevailing at Yucca Mountain (and probably other fractured rock), seepage is more likely to originate from fractures intersecting the cavities than from rock matrix; next we consider film flow on fracture surfaces to estimate the hydraulic conductivity of fractures as a function of background flux (and matric potential); finally, we plot the unsaturated hydraulic conductivity of the fracture domain weighted by fracture porosity for background fluxes (deep percolation) to obtain estimates of seepage for a range of percolation fluxes.

Analyses of Philip et al. [1989] show that the background percolation flux required for matrix seepage into a waste emplacement drift (based on hydraulic properties summarized in Table 1) is about 7 orders of magnitude higher than required for onset of seepage through fractures intersecting the cavity. The argument is based on the boundary layer approximation for cylindrical cavities [Philip et al., 1989] where the maximum dimensionless matric flux potential (ϑ_{max}) for a cylindrical cavity is approximated as:

$$\vartheta_{max} = 2s + 2 - \frac{1}{s} + \frac{2}{s^2} \tag{7}$$

where s=αl/2, with α is the sorptive length and is related to the van Genuchten parameter α_{vg} (we assume equivalence between the parameters for simplicity), and l is the radius of the drift (~ 2 m). Using reported values of α_{vg} for the matrix and fractures, and the relationships between ϑ_{max} and critical percolation threshold (q_0^*) given by [Philip et al., 1989]:

$$q_0^* = \frac{K_s}{\vartheta_{max}(s)} \tag{8}$$

where K_s is the saturated hydraulic conductivity, we obtain a value of ϑ_{max} for rock matrix of 263 [-], and for a mean fracture aperture of 150 µm we obtain ϑ_{max} =16 [-]. Considering the respective permeabilities of matrix and fractures given in Table 1, we immediately find the ratio of $q_{0\ matrix}^*/q_{0\ fracture}^*=5\times10^{-8}$. This result confirms that the capillary retaining force of fractures is smaller than that offered by rock matrix pores. The simplifying representation of fractures using a single sorptive length parameter α_{vg} and permeability yields a significant difference in percolation threshold of more than 7 orders of magnitude between matrix and fracture domains thereby justifying the focus on fracture behavior in subsequent seepage analyses. Note that we are not considering the matrix as impervious as often postulated in single continuum discrete fracture models [Finsterle et al., 2003], rather, we consider the matrix carrying capacity of percolation flux in the "far field" away from the cavity wall, and neglect its contribution to seepage estimation (based on the results above).

Summarizing, seepage through the matrix at low background fluxes is restrained by strong capillary forces [Philip, 1990]; hence, most of the non-diverted flow occurs through hydraulically active fracture surfaces. We recognize that a fraction of the flow is diverted laterally according to the so-called seepage exclusion theory [Philip et al., 1989, Knight et al., 1989, Philip, 1990]. We note however, that in presence

of fractures oriented along the drift axis intersecting the drift (denoted as axial-fractures) they would collect a portion of the laterally-diverted flow (even through the matrix), thereby enhancing the fraction of seepage entering the drift. Therefore, the results of our analysis should be viewed as lower estimates for actual seepage.

Dani Or

07/26/04 - Calculating Seepage Fraction for a Percolation Flux

The primary steps in obtaining an estimate of seepage as a fraction of a given background percolation flux are as follows:

(1) Use physical and hydrologic information to estimate pore size distributions for the dual-continuum FPM model.

(2) Construct the unsaturated hydraulic conductivity constitutive relation for the fractured porous medium.

(3) Assuming flow under a unit gradient, equate the composite hydraulic conductivity to the steady background percolation flux (invoking Buckingham-Darcy's law).

(4) Finally, plot the background flux vs. fracture domain only hydraulic conductivity (uniquely related via matric potential) to establish the relationships between background percolation flux and seepage rates entering the drift.

Remark:

- The calculations for seepage fractions were programmed in MS-Excel 2002. A sample work sheets (tsw35_seepage_master.xls) is archived under C:\SCI_NOTE_SEEPAGE\ . This file was also read by MS-Excel 97 SR-2, and no differences were found.

The physical input parameters from Topopah Springs lower lithophysal formation and estimated pore and fracture aperture size distributions are summarized in Table 1. To be consistent, matrix and fracture hydraulic properties taken from property sets used in dual-continuum models. Note that models of Finsterle [2000] and Finsterle, et al. [2003] are single continuum models where the effect of a range of flow processes, grid resolution, and test conditions are lumped into one of the van Genuchten unsaturated zone coefficients. Thus, property values from Finsterle [2000] were not utilized in our model. The matrix properties in Table 1 are derived from the measurements on cores reported in Flint [1998] and are approximately consistent with calibrated values in the dual-permeability models of BSC [2003b]. The fracture hydraulic properties are taken directly from dual-permeability model calibrations described in BSC [2003b]. The use of calibrated values for fracture unsaturated zone properties is necessitated by the lack of direct measurements, though the fracture permeability values are supported by air permeability measurements. The size distribution of matrix pores was constrained by the reported van Genuchten [1980] parameters. In other words, the matrix pore size distribution was estimated to match the retention curve and was then used to derive the matrix hydraulic conductivity. For the fractures, we selected a fracture aperture distribution that preserved the porosity and closely matched the measured saturated permeability value. The results of this characterization step are depicted in Fig.3 showing the composite hydraulic conductivity function for the fractured porous medium and individual contributions from different domains and flow regimes. Invoking the assumption that a background percolation flux at large depths is primarily gravity-driven (i.e., unit gradient), establishes formal equivalence between the background flux and FPM unsaturated hydraulic conductivity. This means that for any value of percolation flux, we use Fig.3 to identify a particular value of ambient matric potential prevailing in the rock.

Table 1: Model input parameters based on Topopah Springs lower lithophysal data

FRACTURES		
Property	*Value*	*Unit*
Effective (Mean) Aperture	0.031	[mm]
Minimum Aperture	0.000001	[mm]
Maximum Aperture	15	[mm]
Aperture Distribution Parameter ξ	2	
Aperture Distribution Parameter ω	1.03E-05	
Variance	3.2E-10	
Porosity	0.0096	
Van Genuchten Parameter α_{VG}	1.02E-04	$[Pa^{-1}]$
Van Genuchten Parameter α_{VG} (converted to J/kg)	1.02E-01	$[J/kg]^{-1}$
Van Genuchten Parameter m_{VG}	0.633	
Saturated Permeability k_F	9.12E-13	$[m^2]$
MATRIX		
Porosity	0.131	
Van Genuchten Parameter α_{VG}	2.73E-06	$[Pa^{-1}]$
Van Genuchten Parameter α_{VG} (converted to J/kg)	2.73E-03	$[J/kg]^{-1}$
Van Genuchten Parameter m_{VG}	0.227	
Saturated Permeability k_F	7.08E-18	$[m^2]$

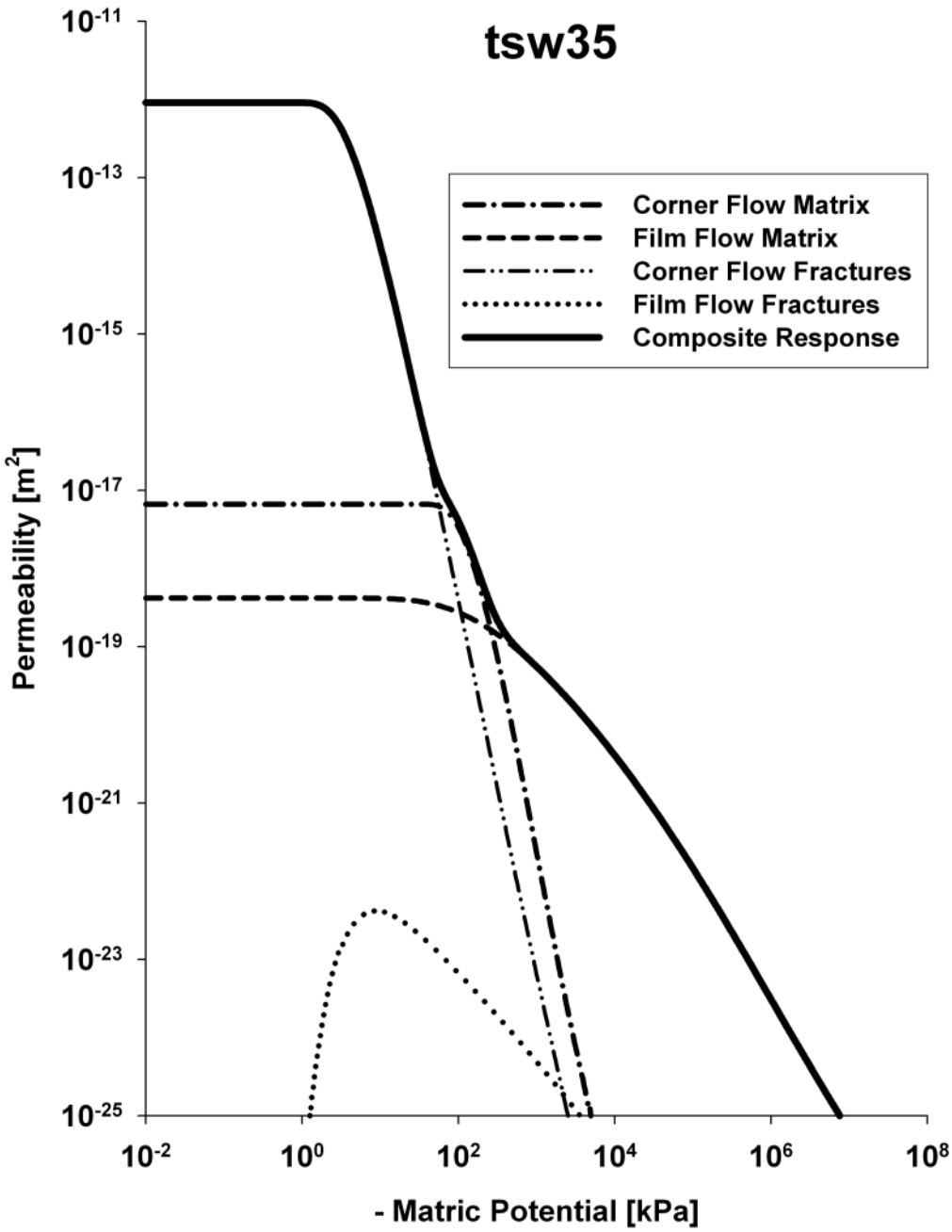

Fig.3: Composite hydraulic conductivity function for fractured Topopah Spring Tuff lower lithophysal formation (following derivations in Or and Tuller [2003]).

Next we plot percolation flux (or composite hydraulic conductivity for unit gradient) versus the hydraulic conductivity of the fracture domain to define the relationships between background percolation flux (independent variable) and seepage flux as depicted in Fig.4a. To examine the sensitivity of the calculations to errors in measured fracture domain permeability, we plot calculations based on a value of fracture permeability that is 10 times the measured value (i.e., 9.12 x 10^{-12} m^2). Finally, to represent the results in a similar fashion as reported by Finsterle [2000], we re-plot the relationships in Fig.4a by scaling the seepage by percolation value as depicted in Fig.4b.

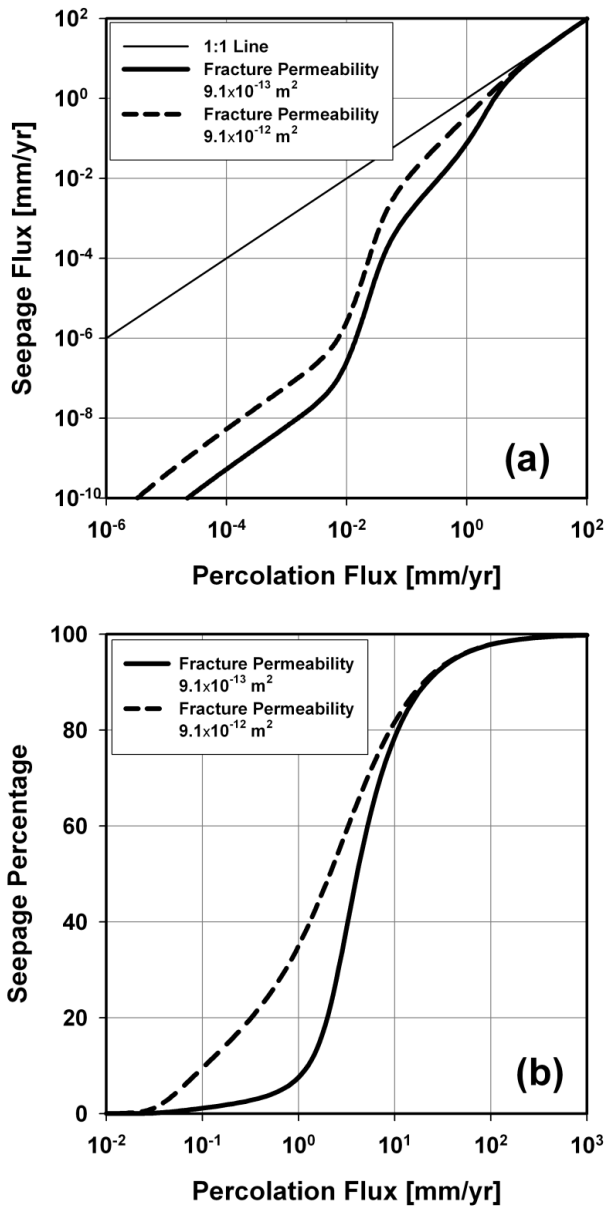

Fig.4: (a) Relationships between average deep percolation flux and seepage flux for Topopah Springs lower lithophysal formation (dashed line for 10 times measured fracture permeability); and (b) relationships between percolation flux and seepage percentage (same data as in Fig.4a).

The results of this simplified analysis show the presence of a seepage threshold in which seepage flux becomes negligibly small for percolation fluxes of less than a few mm/yr. Higher fracture permeability seems to lower the seepage threshold perhaps due to the presence of larger fractures with lower capillary restraining forces promoting early onset of seepage.

Dani Or

08/02/04 - Comparisons with Previous Models and Sensitivity Analyses

The model results were compared with Finsterle's [2000] calculations as depicted in Fig.5. We used two different values of rock matrix permeability due to the large range of values reported in the literature and the uncertainty concerning the influence of background percolation flux. In other words, it is not certain if the seepage-governing flux is the "local" near-cavity flux or a flux determined in formations above the drift

level. Using a value for matrix permeability of 7.1×10^{-18} m^2 [Flint, 1998] for the Topopah Springs lower lithophysal results in considerable differences with Finsterle's [2000] calculations. This value of the matrix permeability is approximately the same as the model calibrated value reported in BSC [2003b]. Finsterle [2000] predicted a seepage threshold value of 15 mm/yr whereas our model predicts a threshold value in the range of 2-4 mm/yr. A better agreement is obtained with the mean value for all formations measured by Flint [1998], which is an order of magnitude higher than the value for the Topopah Springs lower lithophysal formation shown in Table 1). Although the threshold value may be dependent on assumptions regarding fracture porosity and matrix permeability as illustrated next, a more significant difference arises with the rate of reduction (or increase) in seepage with reduction in percolation flux, which is much steeper based on our calculations. The results suggest that for very low percolation fluxes the fraction of flow carried by films and corner flow on fracture surfaces becomes negligibly small and may not give rise to a significant seepage flux.

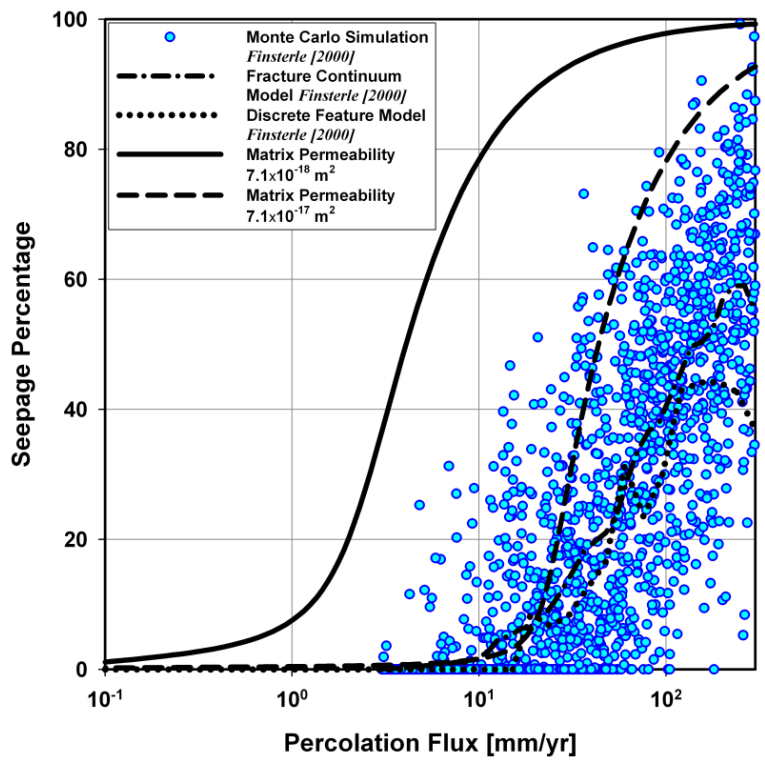

Fig.5: Comparison of new model predictions assuming two values of matrix permeability with Finsterle's [2000] results based on Monte Carlo simulations using fracture continuum (FCM) and discrete feature (DFM) models (lines represent mean values).

Due to the large uncertainty in porosity and permeability of the two domains in the fractured porous medium, we evaluate the sensitivity of the results to variations in key physical properties of the fractures and the matrix. We recalculate the composite relative permeability (i.e., percolation flux under unit gradient) for a range of fracture and matrix porosities.

Sparse data are available to support estimates of aperture distribution at Yucca Mountain or elsewhere. Wilson et al. [1993] used borehole fracture spacing and air permeability data combined with the cubic law for flow in a fracture plane to generate Monte Carlo realizations of aperture distribution following the beta function. They estimated a minimum, mean, and maximum aperture of 0.064, 0.18, and 1.14 mm. Using a similar approach, though absent the Monte Carlo analysis, and data from the ESF and ECRB, CRWMS M&O [2000] estimated mean apertures of 0.098 to 0.16 mm for potential repository horizons. While being cognizant of the cubic law approaches, we integrated maximum aperture data collected in fracture surveys along the ESF tunnel and ECRB drift [Albin et al., 1997; Mongano, et al., 1999] into a constraint of the fracture aperture distribution. A cumulative density function generated for the lower lithophysal unit indicates that 95 percent of the non-zero maximum apertures are less than 15 mm; zero entries for

maximum aperture, which comprise over half of the data, were recorded for fractures below the measurement threshold of approximately 1 mm. Uncertainty in the fracture aperture distribution was further constrained by adjusting the limits of fracture aperture distribution to minimum and maximum values of 0.0001 and 15 mm while matching measured fracture domain permeability given in Table 1. The mean value of the fracture aperture distribution shown in Table 1 is 0.031 mm, which is slightly smaller than the hydraulic aperture estimates estimated by Wilson, et al. [1993] and CRWMS M&O [2000]. Model calculations reveal that under unsaturated conditions the results were not sensitive to upper and lower bounds of aperture size distribution (other than the expected impact on permeability at saturation of larger apertures). This is primarily due to the dominance of liquid films and surface crevices in carrying the flow under unsaturated conditions.

We already discussed the impact of variations in fracture domain permeability of one order of magnitude (see Fig.4). The impact was manifested primarily in the low percolation/seepage values and vanished with increasing percolation flux. Next, we varied porosities of fracture domain and of rock matrix around their nominal values (Table 1) and their impact on the composite permeability of the fractured porous rock as depicted in Fig.6.

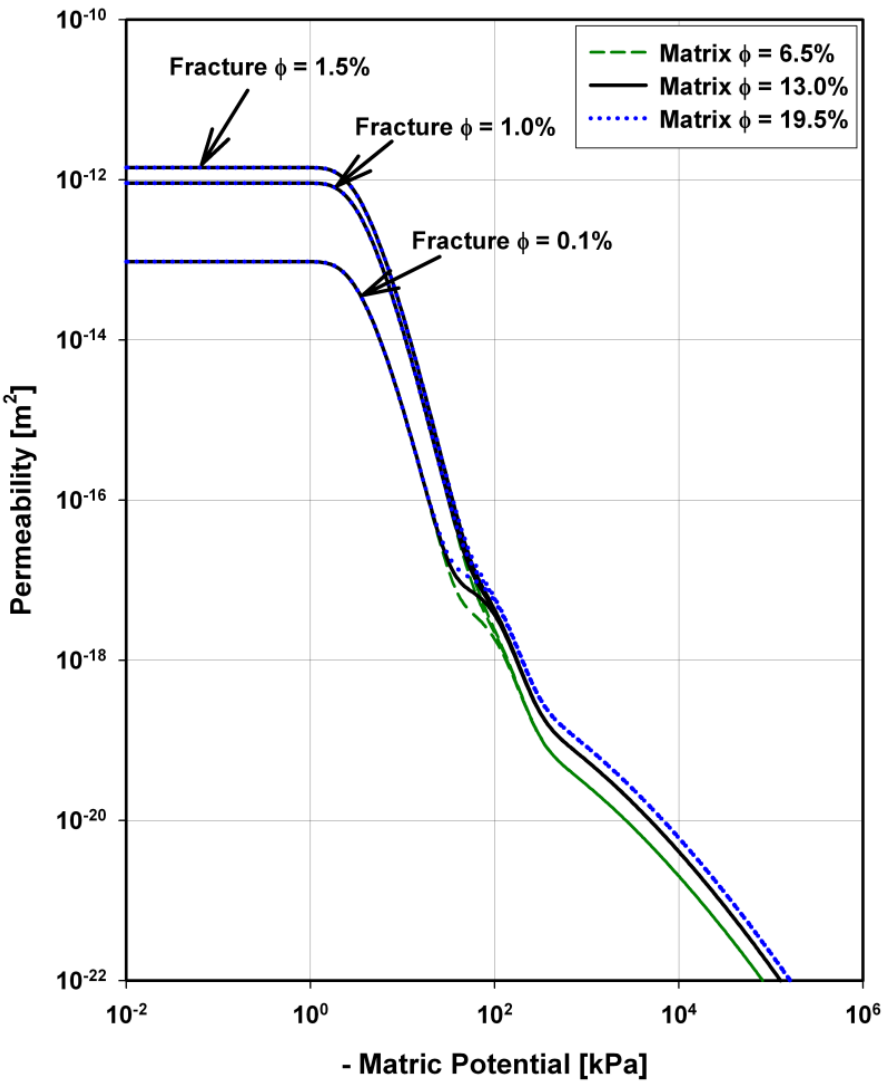

Fig.6: Composite unsaturated hydraulic conductivity function for fractured Topopah Springs lower lithophysal formation for three values of fracture domain porosity, and three rock matrix porosity values (around measured nominal values) as indicated by different lines.

The results clearly show the effect of increasing fracture porosity on the value of permeability near saturation (the highest change). The impact on seepage is likely to be manifested at very high percolation fluxes where seepage threshold is maximal anyway. The effect of varying matrix porosity is reflected at the permeability function at the drier range (matric potential > 3 kPa). Note that the three fracture porosities are indistinguishable at the dry range (they collapse to one curve). Conversely, the three matrix porosities (for each fracture porosity value) are indistinguishable at the wet end.

The relationships between percolation flux and seepage flux for three matrix porosities are depicted in Fig.7. The results show lack of sensitivity to changes in fracture domain porosity these were manifested only at very low percolation fluxes of less than 10 mm/yr. The differences between various fracture porosities are negligible, whereas the effects of different matrix porosity are pronounced. The results indicate that reducing the matrix porosity to 0.065 shifts the percolation threshold for onset of seepage flux to less than 5 mm/yr. This could be important because some rock matrix porosity measurements of cores from potential repository horizons at YM are in the range of 5%. The results suggest that with the reduction in matrix porosity more of the flux is carried through the fracture system (in essence it is being locally diverted to fracture surfaces). Because our interest lies in the drier end, the role of variations in fracture domain porosity is considered marginal.

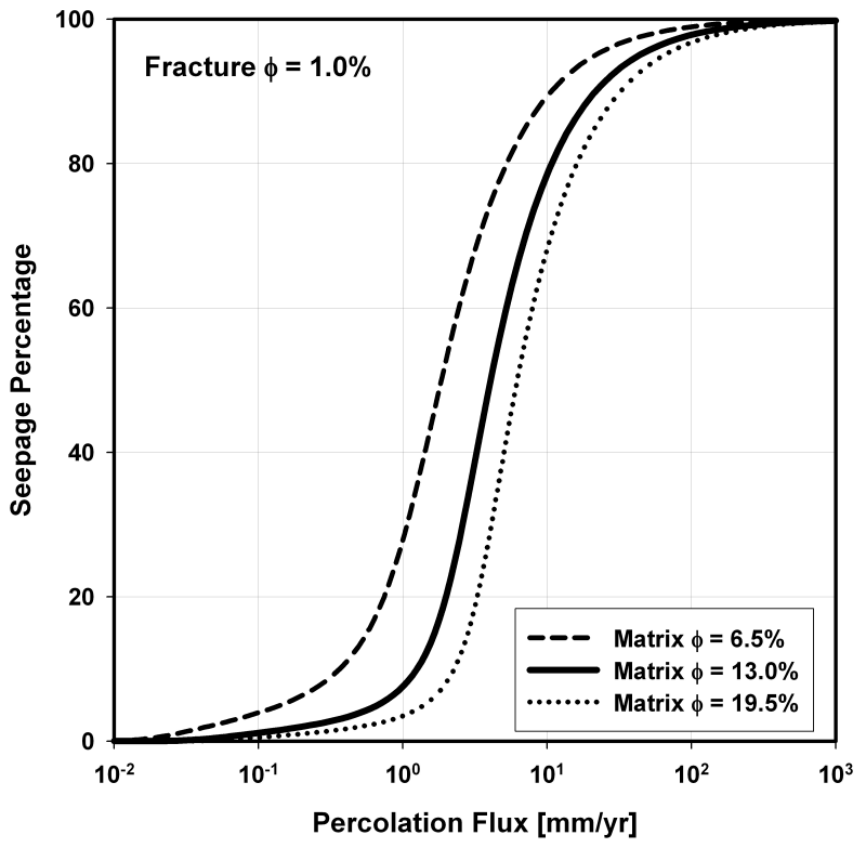

Fig.7: Relationships between percolation flux and seepage percentage for three different values of matrix porosity.

By far the biggest impact on seepage entry to the cavity was induced by changes in rock matrix permeability (Fig.5). This response is significant due to potential impact on seepage prediction at the relatively dry end of practical interest for Yucca Mountain repository design considerations. An increase in (background) percolation flux results in wetter conditions hence lowers ambient matric potential values (closer to zero). The wetter the conditions the larger the fraction of the flux carried by the fracture domain, hence the increase in seepage percentage. This may become even more important at formation interfaces where the fractions between flux carried in the matrix and in the fractures may change significantly.

Remark:

- The sensitivity analysis and comparison with Finsterle's [2000] calculations were performed in MS-Excel 2002. A work sheets (tsw35_sensitivity.xls) is archived under C:\SCI_NOTE_SEEPAGE\ . This file was also read by MS-Excel 97 SR-2, and no differences were found.

Dani Or

08/09/04 – Conclusions and Status

Difficulties in measuring seepage rates at representative locations and at percolation rates and environmental conditions consistent with ambient conditions have led to the reliance of seepage estimates on stochastic numerical models that poorly reflect the physics of the seepage process. To better incorporate the physics of the problem, we introduced a simple approximation for the seepage flux into a cylindrical cavity in a fractured porous medium (FPM) based on standard hydraulic parameters of the FPM and invoking Buckingham-Darcy equivalence between percolation flux and composite hydraulic conductivity under unit gradient (a reasonable assumption for fluxes at large depths). Simple calculations show that seepage into subterranean cavities is dominated by fracture flow due to reduced capillary sorptive length on the one hand and sustainable film flow on fracture surfaces, on the other. Excluding matrix from seepage considerations facilitates estimates of seepage fraction for a given percolation flux considering the hydraulic conductivity of the fracture domain only. We note that this provides a lower estimate of actual seepage due to the potential of axial fractures to intercept laterally diverted flux thereby enhancing seepage.

Calculations show existence of a percolation threshold below which seepage becomes negligibly small. The results also show a steeper increase in seepage with increasing percolation flux, reflecting the "physics" governing fracture film flow, compared to results from equivalent porous medium representations of the FPM, such as the FCM with random heterogeneity of fracture permeability or the DFM with spatially correlated heterogeneity delineating a fracture network [Finsterle, 2000; Finsterle, et al., 2003].

The estimates do not require details regarding fracture network topology in contrast to discrete fracture models and similar methods cited paucity of fracture network information as a major impediment to establishing physically sound seepage estimates. Recognizing that distribution of fracture orientations is likely to play a major role in determining the percolation flux diversion, additional information on fracture orientation should help in quantifying relationships between orientation and position (relative to drift axis) of intersecting fractures and diversion efficiency. We postulate that the presence of axially-oriented fractures (with large apertures) would block and trap lateral diversion of fluxes thereby increasing the amount of seepage. Due to the sensitivity of seepage threshold to small variations in matrix porosity, data on the porosity of the rock forming the ceiling of the drift should improve the analysis. While our estimates of seepage do not require detailed descriptions of fracture characteristics, uncertainty in fracture aperture distribution could readily be reduced by measurements made at the drift wall, or cavity surface. The important fracture characteristics are those at the two-dimensional surface along the cavity wall, not the more difficult to obtain properties of the three-dimensional fracture system of the wall rock. If fracture aperture distributions are difficult to directly measure with sufficient accuracy, correlation of aperture size with another fracture characteristic (e.g., fracture length) may provide an avenue for additional support of aperture distributions used in our model.

The proposed analysis provides the following distinct advantages when compared to FCM and DFM computations:

(1) Analytical solutions – calculations can be simply performed with common spreadsheet software.

(2) More realistic treatment of flow phenomena within the matrix and fracture domains due to consideration of film and capillary flow processes.

(3) Detailed topological characterization of the fracture network is not required. Information on aperture size distribution at the cavity wall, fracture porosity, and saturated fracture permeability are sufficient for fracture domain model parameterization.

A paper on "Seepage Threshold into Subterranean Openings in Fractured Rock" is in preparation for journal submission (Water Resource Research) and started on the CNWRA technical and programmatic process. Hence, it is a good idea to re-assess at this point the status of the work and where it may be heading.

9/29/04 - Open issues (pertaining to the KTI) for future model improvement

- A more in-depth evaluation of 3-D flow pathways would enhance our confidence in the simplifying assumptions made in this study.
- Data for "predictive testing" of model predictions from injection tests would be a logical next step to independently verify model performance.
- The abundance and role of "axial fracture" must be incorporated in future discussions concerning seepage exclusion – regardless of the model type.
- The assumed roughness geometry does not consider asperities and similar elements rising above mean fracture surface plane. Introduction of such elements should add realism to the model and capture some of the intermittent flow behavior observed. For inclusion of these elements we need to consider liquid build-up around conical objects (see "edge" in Appendix B of Tuller et al., 1999).
- The dynamics matrix-fracture interactions were not treated in this work – some of the rates of such interactions would be useful to capture the essence of potential bypass flow through these fracture surfaces (e.g., as liquid flux encounter low porosity/permeability layer such as the PTN).

References

Albin, A.L., W.L.Singleton,; T.C. Moyer, A.C. Lee, R.C. Lung, G.L.W. Eatman, and D.L. Barr, Geology of the Main Drift - Station 28+00 to 55+00, Exploratory Studies Facility, Yucca Mountain Project, Yucca Mountain, Nevada. Milestone SPG42AM3. Denver, Colorado: Bureau of Reclamation and U.S. Geological Survey. 1997.

BSC, In Situ Field Testing of Processes. ANL-NBS-HS-000005 REV02. Yucca Mountain Project, Las Vegas, NV: Bechtel SAIC Company, LLC. 2003a.

BSC, Calibrated Properties Model. MDL-NBS-HS-000003 REV01. Yucca Mountain Project, Las Vegas, NV: Bechtel SAIC Company, LLC. 2003b.

CRWMS M&O, Analysis of Hydrologic Properties Data. ANL-NBS-HS-000002 REV00. Yucca Mountain Project, Las Vegas, NV: Civilian Radioactive Waste Management System, Management and Operator. 2000.

Finsterle, S., Using continuum approach to model unsaturated flow in fractured rock. *Water Resour. Res. 36*, 2055-2066, 2000.

Finsterle, S., C.F. Ahlers, R.C. Trautz, and P.J. Cook, Inverse and predictive modeling of seepage into underground openings. Journal of Contaminant Hydrology 62/63:89- 109, 2003.

Flint, L., Characterization of hydrogeological units using matrix properties, Yucca Mountain, Nevada. *Water-Resources Investigations Report 97-4243*. Denver, CO: U.S. Geological Survey. 1998.

Hughson, D.L., Dodge, F.T., The effect of cavity wall irregularities on seepage exclusion from horizontal cylindrical underground openings. J. Hydrol. 228, 206–214, 2000.

Knight. J.H., J.R. Philip, and R.T. Waechter, Seepage exclusion problem for spherical cavities, *Water Resour. Res. 25*, 29-37, 1989

Mongano, G.S., Singleton, W.L., Moyer, T.C., Beason, S.C, Eatman, G.L.W., Algin, A.L., and Lung, R.C., Geology of the ECRB Cross Drift - Exploratory Studies Facility. Yucca Mountain Project Milestone SPG42GM3, Denver, CO: U.S. Geological Survey. 1999.

Or, D. and M. Tuller, Liquid retention and interfacial area in variably saturated porous media: Upscaling from pore to sample scale model, *Water Resour. Res., 35*(12), 3591-3605, 1999.

Or, D. and M. Tuller, Flow in unsaturated fractured porous media: Hydraulic conductivity of rough surfaces, *Water Resour. Res., 36*, 1165-1177, 2000.

Or, D., and M. Tuller, Hydraulic conductivity of unsaturated fractured porous media: Flow in a cross-section. Adv. Water Resour., 26(8):883-898, 2003.

Philip, J.R., J.H. Knight, and R.T. Waechter, Unsaturated seepage and subterranean holes: Conspectus, and exclusion problem for circular cylindrical cavities. *Water Resour. Res. 25:*16-28, 1989.

Philip, J.R., Some general results on the seepage exclusion problem. *Water Resour. Res. 26*:369-377, 1990.

Tuller, M., D. Or, and L.M. Dudley, Adsorption and capillary condensation in porous media: Liquid retention and interfacial configurations in angular pores, *Water Resour. Res., 35*(7), 1949-1964, 1999.

van Genuchten, M.T., A closed-form equation for predicting the hydraulic conductivity of unsaturated soils, *Soil Sci. Soc. Am. J., 44,* 892-898, 1980.

Wang, J.S.Y., and T.N. Narasimhan, Unsaturated flow in fractured porous media, In: Bear, J., Ch-F. Tsang, and G. De Marsily (Editors), Flow and contaminant transport in fractured rock, *Academic Press Inc.,* 325-394, 1993.

Microtensiometry for determination of relative humidity of air near saturation

Collaborators: Markus Berli (UConn), Jon Drasdis (UConn)

Directories: C:\Documents and Settings \mberli \My_Documents \my_job \Current_Projects\RH_Sensor\

Objective of this study:

To explore the potential of using micro-tensiometers to determine relative humidity of nearly water-vapor saturated air (99.95 to 100 % RH) and track minute changes in relative humidity in drifts and "cold trap" experiment.

04/14/04 – Initial entry

Dani Or

The Study was initiated to overcome limitations in using present methods of relative humidity (RH) measurements as part of the "cold trap" and related experiments conducted under very high RH values close to 100%. Motivated by the need to accurately measure minute changes in RH near saturated values, we embarked on development of simple and cheap sensor that could bridge the existing measurement gap. The basic idea was to use a tensiometer consisting of a water-filled tube connected to saturated porous cup that could exchange water with the wet/dry air while maintaining tension in the system measured by sensitive pressure transducer. The so-called Kelvin's equation establish direct relationships between the tension in the tesniometer and the air RH in equilibrium with the tensiometer.

Several key processes in multi-phase environmental systems such as water condensation, corrosion, and most aspects of microbial activity require very high relative humidity (RH) of the ambient air. Despite the wide spread and importance of these processes currently available RH sensors become progressively inaccurate close to saturation and typically are unable to resolve RH in the range of 99.95 to 100 % where most water-related biological and phase change processes take place. To circumvent this measurement gap we propose a different approach to measurement of relative humidity, one that is based on tensiometric measurement of water pressure in porous system that is exposed and attains equilibrium with the air mass of interest. For the range of RH near saturation we exploit the relationships between relative humidity and water potential according to the well-known Kelvin equation.

A relative humidity value of 100% corresponds to a water potential of 0 Pa with decreasing water potential as relative humidity decreases. Water potentials in the range of -8×10^4 to 0 Pa (which corresponds to relative humidity between 99.95 and 100 %) can be easily determined using a tensiometer, a well-established technique to measure matrix potentials of soil water. Therefore we suggest using a tensiometer as a sensor to determine relative humidity close to water saturation.

The objective of this study was to explore the potential of a micro-tensiometer to determine relative humidity of nearly water saturated air (99.95 to 100 % RH). We suggested therefore to proceed as follows:

Step #1: (a) Build a micro tensiometer to measure relative humidity in the range of 99.95 to 100 %, (b) determine air water potentials within the range of 0 to –800 mbar, (c) evaluating different designs for the probe tip

Step #2: Develop an experimental setup to monitor and control RH in the desired range.

Step #3: Calibrate and validate the sensor using air with defined relative humidity.

Dani Or

04/16/04 – A brief overview of relative humidity, water potential and tensiometry

For completeness we review important aspects of relative humidity of water in air and introduces its relations to temperature, water activity and water potential used in this study to determine relative humidity from water potential measurements.

Relative humidity and water activity

The relative humidity (RH) of water in air is defined as

$$RH = 100 \frac{p}{p_0} \text{ [\%]} \tag{1}$$

with p the actual vapor pressure and p_0 the vapor pressure for water saturated air. Vapor pressure and relative humidity of air are functions of temperature, related according to the Clausius-Clapeyron equation

$$\frac{d(\ln p)}{dT} = \frac{\Delta H_{vap}}{RT^2} \tag{2}$$

with p the vapor pressure [Pa], T the (absolute) temperature [K], ΔH_{vap} the enthalpy of vaporization (for water: 40.67 kJ mol^{-1}) and R the molar gas constant (8.31 J mol^{-1} K^{-1}). Solutions of the Clausius-Clapeyron equation (2) for water are shown graphically in Fig. 1

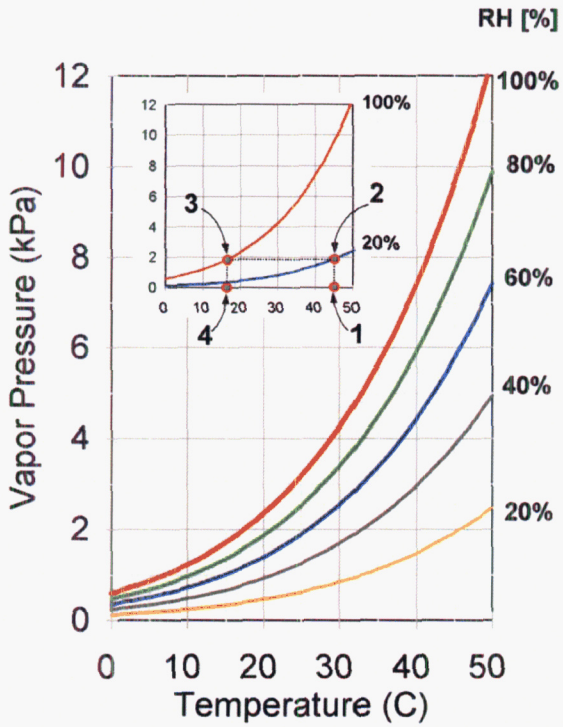

Fig. 1: Vapor pressure of water and relative humidity in air as a function of temperature.

The insert in Fig. 1 illustrates the steps for determining actual water vapor pressure, p, for temperature T = 45° C and relative humidity RH = 20% (1&2); the corresponding saturation vapor pressure, , and associated dew point temperature (3 & 4). The relationships between *p, T and RH* are uniquely defined, hence knowledge of any two defines the third quantity. The vapor density ρ_v (mass of water per unit volume of air) can be expressed, based on the ideal gas law, as a function of vapor pressure, p, and temperature, T, according to

$$\rho_v = \frac{p}{4.26 \times 10^2 \; T} \tag{3}$$

For our previous example (T = 45° C and RH = 20%), the vapor pressure is p = 2 kPa which yields a vapor density ρ_v = 1.6×10^{-2} kg m^{-3}.

For air in equilibrium with an aqueous salt solution, RH is equivalent to the water activity, a_w, of the solution which can be expressed as

$$RH = 100 \; a_w = 100 \; \lambda_w \; x_w \tag{4}$$

with λ_w the activity coefficient of water and x_w the molar fraction of water in the aqueous phase. For solutions with water activity a_w > 0.95, one can assume $\lambda_w = 1$. For the relative humidity of air above pure water (salt concentration in the solution = 0), we obtain RH = 100% since the molar fraction x_w = 1 and hence the water activity a_w = 1. The molar fraction of water, x_w, in the solution and the relative humidity, RH, in the air decrease with increasing salt concentration. We take advantage of this simple relation between RH and x_w to achieve in a batch experiment an air atmosphere of defined RH over a salt solution by controlling x_w of the salt solution. For details and an example for calculation of RH over potassium chloride (KCl) solution, see Appendix 1.

Relative humidity and water potential - Kelvin's equation

Relative humidity RH and water potential Ψ are related with Kelvin's equation (5) (Thomson, 1871) according to

$$RH = 100\ Exp\left(\frac{M_w\ \Psi}{\rho_w\ R\ T}\right)\ [\%] \qquad (5)$$

with M_w the molar mass of water [kg mol^{-1}], ρ_w the density of water [kg m^{-3}], R the molar gas constant (8.31 J mol^{-1} K^{-1}) and T the (absolute) temperature [K]. Equation (5) is used to relate the measured water potentials Ψ with the relative humidity, RH, of the air.

Water potential measurement - tensiometry

The soil water matric potential (a component of total water potential) is often determined with the use of a device known as a tensiometer. It consists of a saturated porous cup in hydraulic contact with soil water connected through a water-filled tube to a pressure/vacuum gauge (Fig. 2a) that allows direct readout of soil water tension (subatmospheric pressure). When soil in contact with the cup is dry, water flows our of the tensiometer until the internal suction opposes the "pull" of the soil – the tensiometer reads the soil water matric potential. For additional information regarding water potential determination and tensiometer types we refer to Hillel (1998) or Jury et al. (1991)

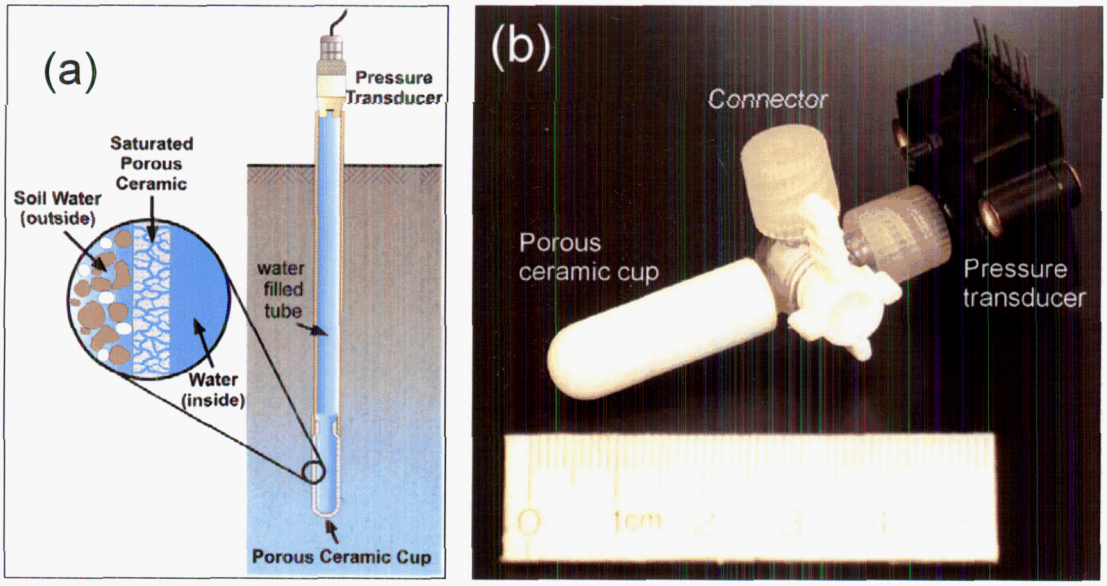

Fig. 2: (a) tensiometer used to measure matrix potentials in soil; and (b) a micro-tensiometer, developed in this study to measure water potentials in air.

05/01/04 - Sensor design and data acquisition

Dani Or

In a first step, we built a micro-tensiometer as a basic "platform" for our relative humidity sensor to measure water potentials within the range of 0 to –800 mbar which correspond to relative humidity in the range of 99.95 to 100 %. The micro-tensiometer consisted of a porous cup filled with water and hydraulically connected to a pressure transducer (type PX 137-015DV, Omega Engineering) that allows electronic readout of pressures in the range of ± 1 bar relative to prevailing atmospheric pressure (Fig. 2b). For pressure monitoring and data acquisition, a data logger (type CR23X, Campbell Scientific) was used.

In our preliminary experiments, sensors with tips of different materials including, thick- and thin-walled ceramic as well as stainless steel were tested (Fig. 3). All three types of tips were capable of measuring water potential in air, however, it became apparent that each came with its own limitations. The stainless steel tip showed very fast response to potential changes but failed to measure potentials lower than –60 mbar due to its low air entry value (air bubbled in a disrupted tension measurement). The ceramic tips could sustain potentials as low as –800 mbar but suffered either from a very slow response to potential changes (the thick-walled tip), or from had such limited water capacity (thin-walled tip) that it would quickly dry and lose functionality. Since capability of measuring large potential range emerged as the most important criteria for a successful application of the micro-tensiometer for relative humidity measurements, we decided proceed with ceramic tips (Fig. 3 a and b) for our sensor.

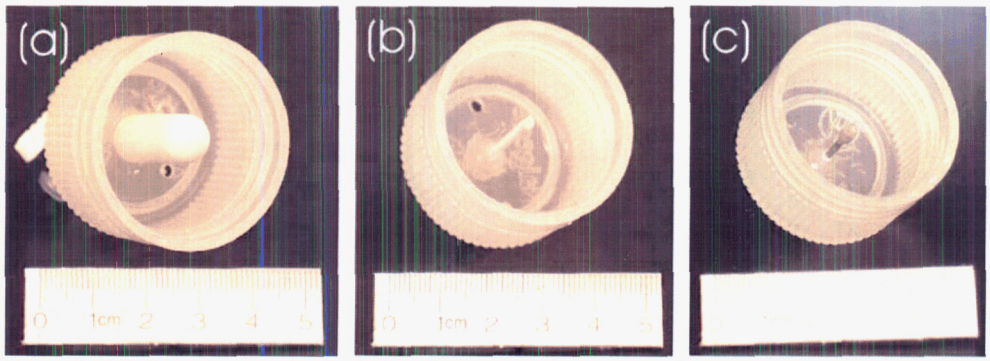

Fig. 3: Probe tips selected for the experiments: (a) thick- and (b) thin-walled ceramic, (c) stainless steel.

05/04/04 – Control of relative humidity in ambient air

Dani Or

In subsequent steps we used a container with controlled relative humidity in the head space for calibrating the our relative humidity sensor. In a first attempt a dew-point generator (type LI 610, LI COR) connected to a flow cell was used. Within the flow cell, relative humidity was monitored by a relative humidity transmitter (type HMP243, Vaisala). We found that the transmitter could not read relative humidity values >96% and the dew point generator could not control relative humidity within the accuracy needed. Therefore we decided to use salt solutions of known water activity to calibrate our relative humidity sensor. Potassium chloride (KCl) solutions of different molality were prepared following Wiebe et al. (1971). The solutions were filled in plastic flasks, which were sealed with a cab with the sensor attached to it (see
Fig. 4). Molalities of the KCl solutions and their related water potentials and relative humidity values are given in Table 1. For details with regarding the relation between water potential and molality see equations (4), (5) and Appendix 1.

Table 1 Molality of KCl solution, related water potential and relative humidity

Molality [mol KCl kg^{-1} H_20]	Water potential [mbar]	Relative humidity [%]
0	0	100
1.21×10^{-3}	-60	99.996
1.51×10^{-3}	-75	99.995
3.03×10^{-3}	-150	99.989
6.06×10^{-3}	-300	99.978
1.21×10^{-2}	-600	99.956

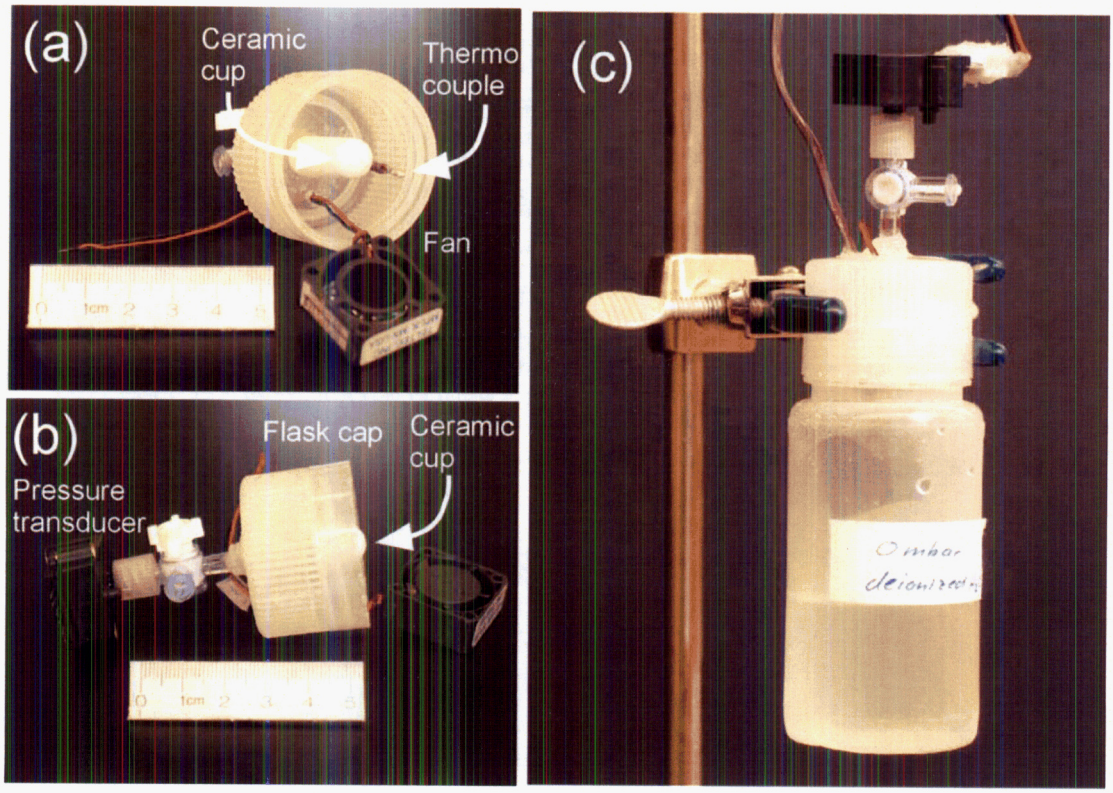

Fig. 4: Front (a) and side view (b) of the micro tensiometer, attached to the cap of a Nalgene flask; (c) complete experimental setup consisting of the micro tensiometer connected to a flask containing deionized water or KCl solution to control water potential in the air above the liquid.

6/01/-7/22/04 - Sensor calibration and testing

Dani Or

As a third step, we tried to calibrate our RH-sensor using air of controlled relative humidity over deionized water and KCl solutions.

Thin-walled sensor no air mixing

We started by measuring water potentials over deionized water and 0.0014, 0.006 and 0.012 M KCl solutions using the new *RH* sensor with the thin-walled ceramic probe tip (Fig. 3b) considering rapid response to be the most important characteristics. The probe tip was initially water saturated and subsequently dried out, as determined by the water potential in the ambient air. Water potentials in the air above the salt solutions were expected to be 0, -60, -300, -600 mbar at steady-state, corresponding to 100, 99.996, 99.978 and 99.956% relative humidity, respectively.

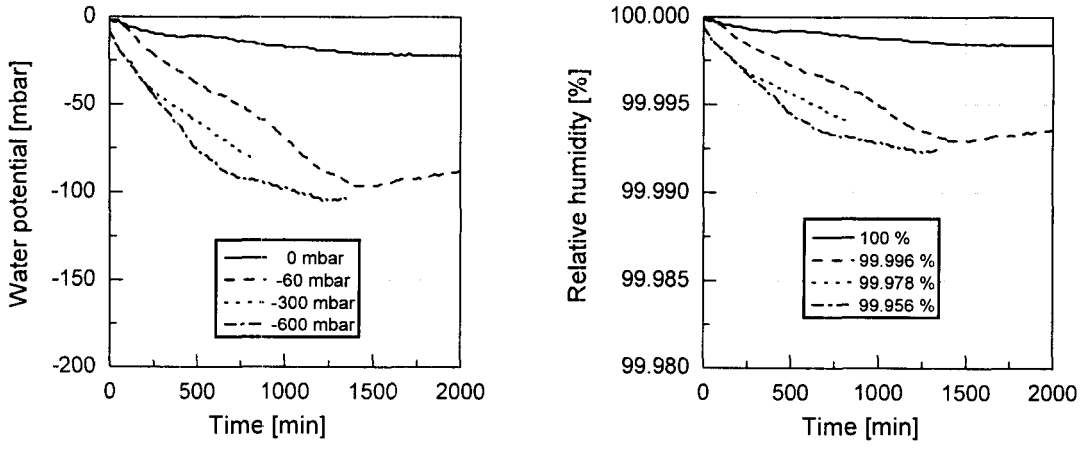

Fig. 5: Measured water potentials and relative humidity in air above deionized water as well as 0.0012, 0.006 and 0.012 M KCl solutions without air mixing using a thin-walled ceramic probe tip.

Water potentials and relative humidity calculated with equation (5) decreased with time and reached steady-state values after about 20h (Fig. 5). Although water potentials and relative humidity measured above the KCl solutions were lower than above deionized water, the values were generally higher than expected for the salt solution used. Above deionized water, we measured water potentials lower than zero and relative humidity values lower than 100%. Despite the considerable differences in salt concentrations in the solutions, the measured water potentials and relative humidity values at steady state were quite similar (around –100 mbar or 99.993%, respectively).
Similar results in different tests led us to conclude that the lack of mixing of the air in the test flask resulted in a boundary layer effect (sa table layer of air of constant water potential around the probe tip) hence we decided to use a fan to mix the air within the flask.

Thin-walled sensor mixing with fan
The use of a small fan resulted for the 0.006 M KCl solution a measured potential that agreed well with the theoretically expected value of –300mbar. For the 0.012 M KCl solution (theoretical potential –600 mbar) the measured value overestimated the theoretical potential considerably as shown in Fig. . In both cases the potentials increased drastically after reaching a potential minimum followed by a sharp increase (Fig. 6) which we associated with air breaking through the ceramic cup. This abrupt drying effect was particularly pronounced with the thin-walled sensor due to the probe tip low water capacity. To avoid air entry before the water potential in the sensor attains steady state values, we decided to use a ceramic tip with a thicker wall (Fig. 3a), and hence higher water capacity, and also adjust the fan running time to optimize the (necessary) drying process.

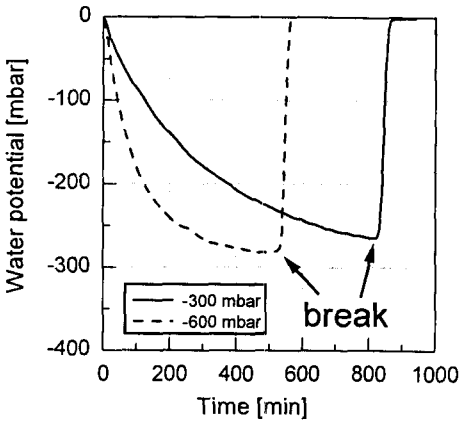

Fig. 6: Water potential and relative humidity above 0.006 and 0.012M KCl solutions using a thin-walled ceramic probe tip and a fan for air mixing.

Thick-walled sensor and the role of air mixing intensity

Using a thick-walled probe tip and varying mixing time (no mixing for 0 and –75 mbar, 1s per minute for –150 mbar, 12.5s per minute for –300 mbar and 30s per minute for –600 mbar), measured water potentials reached steady state values, which agreed quite well with the theoretically predicted ones as depicted in Fig. .

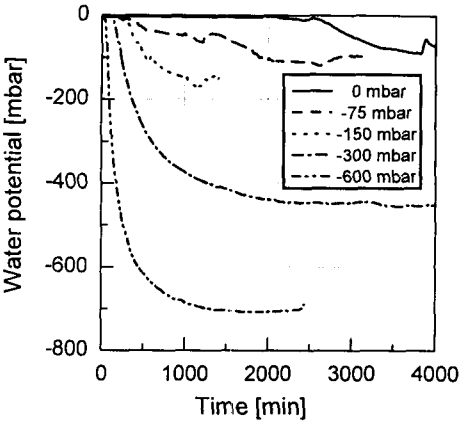

Fig. 7: Water potential above deionized water , 0.0015, 0.003, 0.006 and 0.012M KCl solutions. Measurements were taken with a thick-walled ceramic probe tip and a small fan mixing the air for 1s per minute (0.003M solution), 12.5s per minute (0.006M solution) and 30s per minute (0.012M solution).

The results in Fig. illustrate considerable influence of mixing time on measured water potentials. To test the role of mixing intensity in measured potential (Relative humidity) we conducted tests using a single solution concentration (0.006 M KCl, theoretical potential -300 mbar) but variable mixing times. The experiment yielded potentials between –100 and –700 mbar for mixing times of 1s per minute (1.6% mixing time) up to 30s per minute (50% mixing time) (Fig. 8). It is interesting to note that for too low mixing times, the expected equilibrium value was not reached whereas for too high

mixing times, the resulting potentials and relative humidity eventually reached an equilibrium after an initial overshoot beyond the expected value (Fig. 8, 25% mixing time).

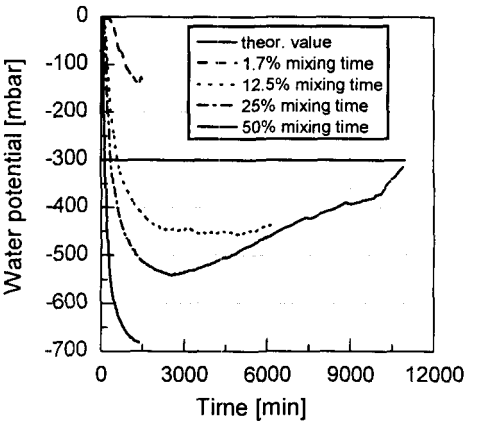

Fig. 8: Water potentials as functions of time for different mixing times over a 0.006 M KCl solution (theoretical potential value: -300 mbar).

Experiments with solutions of different KCl concentrations and equal mixing time (1s per minute) supported the findings depicted in Fig. 8. For deionized water and 0.0015 M KCl solution (-75 mbar), measured potentials were lower and for 0.006 and 0.012M KCl solutions (-300 and -600 mbar) higher than expected (Fig. 9).

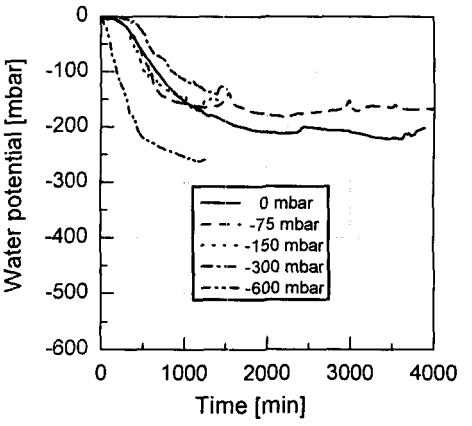

Fig. 9: Water potentials as functions of time for different KCl solution concentrations and a single mixing interval (1/60) of 1s/minute mixing time.

The results from Fig. 5, 8, and 9 indicate that for low potentials (< -100 mbar) mixing of 1 to 30s per minute may be needed, whereas for higher potentials (> -100 mbar) the role of mixing is less important. It is interesting to note that also over pure water, potential and relative humidity drop with time (Fig. 5 and 7) even without air mixing.

Temperature effects - thick-walled sensor
Results of our experiments show the influence of temperature on measured potentials and relative humidity to be surprisingly small (Fig. 10), especially for water potentials close to zero. With decreasing potential (drier air), measured values become more temperature sensitive. It is interesting to see that for short mixing times; measurements seem to reflect higher temperature sensitivity than for high mixing times resulting in smoother potential curves.

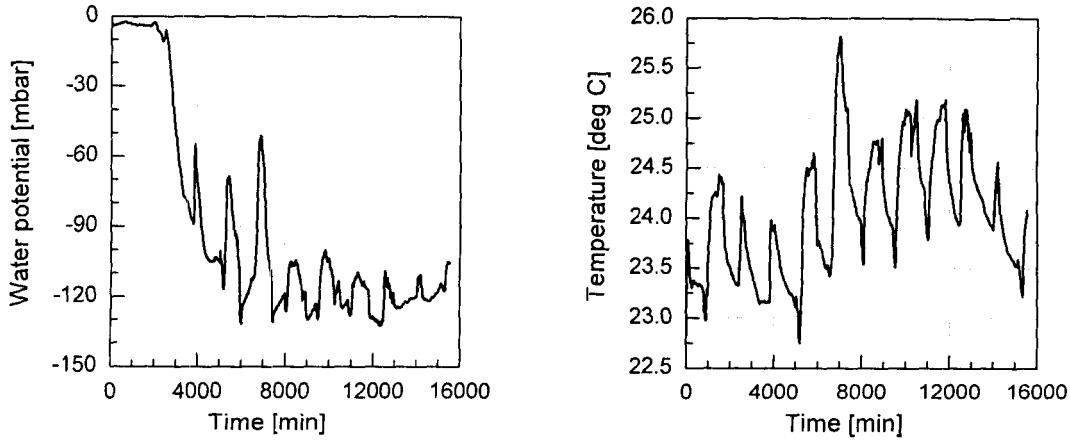

Fig. 10: Influence of temperature on potential measurements over deionized water without mixing.

Summary and conclusion

The study demonstrated the possibility of measuring water potential and application of the Kelvin equation to determination of relative humidity of air close to water saturation using tension measurements in a microtensiometer. Results show that mixing conditions of ambient air at a given RH have considerable influence on measured potential. The sensor reads higher relative humidity values for potentials <-100 mbar if air is not well mixed. For potentials from 0 to -100 mbar, no mixing was needed. For both cases, attainment of equilibrium potential takes a long time (days) before stable state reliable measurements are established. If the water capacity of the probe tip is too small, the probe tip may dry out too fast and no steady state potential may be reached.

Despite limitations of current designs and difficulties in establishing reliable readings, our tests support the working hypothesis that micro-tensiometer is capable of determining relative humidity in air close to water saturation. The results and development of boundary layer (in water saturated porous cup) shed a new light on the rates and limitations to drying of rock surfaces lining unventilated drift – it is clear that indiscriminant application of the Kelvin equation under these conditions must be reviewed carefully.

Open issues for future considerations

- Water potentials lower than zero were measured within a ceramic sensor even for air in equilibrium with deionized water. Assuming that air in equilibrium with pure water is at 100% relative humidity (0 mbar water potential), the causes of a measurable potential difference across the wall of the probe tip must be considered more carefully. This may also represent the specific interactions imparted by the probe porous matrix.
- Considering the importance of air mixing in measured potentials in our experimental system, we should consider alternative testing chamber and probe configuration designs. For example, placing the probe tip in a flow cell connected to a reservoir with known salt solution. The air would flow from the reservoir through a connection to the flow cell and, driven by a fan, back to the reservoir. This may enable better control of air flow and probe tip (controlled flow field of the air).
- The potential for establishment of a boundary layer around water saturated porous cup provide potential insights regarding rates and limitations to drying of rock surfaces lining unventilated drifts. Extrapolating from the microtensiometer behavior in air, it is apparent that the application of Kelvin's equation under these conditions must be viewed with caution and the formation of evaporation retarding boundary layer must be considered in modeling of drying of these surfaces.
- The results of this study highlight the complexity involved in phase change across a porous interface and what seems as a straightforward application of basic thermodynamic principles, was met with considerable complexities (boundary layer, rates of equilibrium, air bubbling, and liquid capacitance). These will provide a new set of criteria for design of the next generation high RH sensor.

References

Hillel, D., 1998. Environmental Soil Physics. Academic Press, San Diego, 771 pp.

Jury, W.A., Gardner, W.R. and Gardner, W.H., 1991. Soil Physics. John Wiley & Sons, New York, 328 pp.

Thomson, W., 1871. On the equilibrium of vapour at the curved surface of liquid. Philosophical Magazine, 42(Dec.): 448-452.

Wiebe, H.H. et al., 1971. Measurement of plant and soil water status, Utah State University, Logan, Utah, Logan.

Appendix 1: Relation between water activity (equivalent to relative humidity) and KCl molality

Source for the water activity definition: http://www.lsbu.ac.uk/water/activity.html

Relative humidity RH is equivalent to water activity, a_w, which can be expressed as

$$RH = 100\, a_w = 100\, \lambda_w\, x_w \tag{6}$$

with λ_w the activity coefficient and x_w the mol fraction of water in the aqueous phase. For water, one can assume $\lambda_w = 1$. For potassium chloride (KCl) dissolved in water, x_w is defined as

$$x_w = \frac{[H_2O]}{[H_2O]+[K^+]+[Cl^-]} \tag{7}$$

with $[K^+]$, $[Cl^-]$ and $[H_2O]$ the concentrations in mol l^{-1} of the species in the aqueous solution. Using the mol masses of water (M_w = 18 g/mol) and KCl (M_{KCl} = 74.55 g/mol), x_w can be expressed as a function of mol masses and the actual water, m_w, and KCl mass, m_{KCl}, according to

$$x_w = \frac{1}{1+2(m_{KCl}\, M_w)/(m_w\, M_{KCl})} \tag{8}$$

For a given relative humidity RH and, hence, given water activity, a_w, and mol fraction, x_w, the molality of KCl (mol KCl kg^{-1} water) is then

$$[KCl] = \frac{m_{KCl}\, M_w\, 55.56}{m_w\, M_{KCl}} = \frac{55.56}{2}\left(\frac{1}{x_w} - 1\right) \tag{9}$$

where 55.56 is the amount of mol water in one kg of water.

ADDITIONAL INFORMATION FOR SCIENTIFIC NOTEBOOK NO. 618E

Document Date:	7/05/2004
Availability:	Southwest Research Institute® Center for Nuclear Waste Regulatory Analyses 6220 Culebra Road San Antonio, Texas 78228
Contact:	Southwest Research Institute® Center for Nuclear Waste Regulatory Analyses 6220 Culebra Road San Antonio, TX 78228-5166 Attn.: Director of Administration 210.522.5054
Data Sensitivity:	■"Non-Sensitive" □ Sensitive □"Non-Sensitive - Copyright" □ Sensitive - Copyright
Date Generated:	10/04/2004
Operating System: (including version number)	Windows
Application Used: (including version number)	
Media Type: (CDs, 3 ½, 5 1/4 disks, etc.)	1 CD
File Types: (.exe, .bat, .zip, etc.)	xls, doc, pdf
Remarks: (computer runs, etc.)	Notebook supplemental material